An Optical Investigation of Thermal Runway Phenomenon Under Thermal Abuse conditions

Antonio García[*], Javier Monsalve-Serrano, Rafael Lago Sari, Santiago Martinez-Boggio

CMT - Motores Térmicos, Universitat Politècnica de València, Camino de Vera s/n, 46022 Valencia, Spain

Energy Conversion and Management
Volume 246, 15 October 2021, 114663
https://doi.org/10.1016/j.enconman.2021.114663

Corresponding author (*):
Dr. Antonio García (angarma8@mot.upv.es)
Phone: +34 963876574

Abstract

This work aims at studying the thermal runaway process caused by thermal abuse using different optical techniques. A commercial Samsung ICR 18650 – 26 J cylindrical battery cell is exposed to different heating ramps in a Continuous Flow Vessel (CFV) to identify critical phases of the battery thermal runaway. The open volume test bed allows to increase the temperature under controlled conditions and evacuate the released gases, enhancing the visualization of the battery venting and combustion. The venting of the electrolyte and gases is seen around 200°C. The safety time, defined as time between venting and fire, was around 3 minutes, with an inverse relation with respect to the heating ramp. The use of fast cameras (schlieren, Natural Luminosity and OH*) allowed to deeply understand the phenomena of liquid electrolyte and generated internal gases venting as well as the combustion process.

Keywords

Battery Thermal Runaway, Lithium Ion Battery, Fire, Safety, Electric Vehicles

1. Introduction

Recently, the International Agency of Energy has provided the roadmap to obtain the carbon neutrality goal in 2050 which was defined in the green deal [1]. One of the most alarming points concerns the urgent ban of new vehicles based on internal combustion engine (ICE) propulsion. Alternatives such as the use of synthetic [2][3] and renewable fuels [4][5] as well as advanced combustion concepts [6][7] may extend the ICE-based vehicle life. Nonetheless, different countries already set their deadline for banning the ICE. This measure intends to shift the road transport sector towards a low carbon footprint economy, having battery electric vehicles (BEVs) as the preferred powertrain for this sector [8][9]. Despite the exponential increase in the sales, these vehicles still represent small market shares around the world, needing additional financial incentives to deploy the required infrastructure to run these vehicles and to guarantee their affordability [10].

Battery application in mobility requires a multidisciplinary approach, involving thermal, electrical, and chemical sciences [11][12]. At the same time, it must be economically viable, which means achieving parity pricing with ICEs vehicles (in $/kWh terms) to assure market acceptance [13]. The battery pack is usually the most expensive component in an BEV and represents approximately 30% to 40% of total cost to consumers [14]. In recent years, a great cost reduction has been accomplished, managing to reduce the battery pack price from 668 $/kWh in 2013 to 137 $/kWh in 2020 [15]. Much of the cost reduction of the battery packs over the last few years is related to swapping 80% of the cobalt with nickel [16][17]. The target set by organisations worldwide is to break the 100 $/kWh barrier in the close future [18][17].

Different chemistries are being used in the automotive sector such as Lithium Cobalt Oxide - $LiCoO_2$ - (LCO), Nickel Manganese Cobalt (NMC) and Lithium *Ferrum* Phosphate (LFP) batteries. In general, the battery cell is distinguished in two main categories, Energy Cells (high capacity expected) or Power Cells (high drawn currents expected). The chemistry will generally be selected according to the cell usage. A chemistry is always a balance between energy, capacity, cycle life and safety. Traditionally, LFP cells have been used for energy storage applications since they are safer and have longer shell lives than any other type of battery [19]. The inconvenient of LFP cells is their low specific energy in comparison to NMC cells [20]. However, LFP cells can be a good option for mid-range EV models once the use of fast charging techniques is supported [21]. As it can be observed in Figure 1, these cathode chemistries will be supporting the electric vehicle market for several years to come, highlighting the importance of assuring proper safety strategies and prolonged battery life. Solid state batteries are suggested to represent a potential solution to obtain high power density and safe operation at the same time [22]. Being referred to as possible generation 4 batteries (beyond 2025), their usage is still restricted to prototypes due to the high production costs associated.

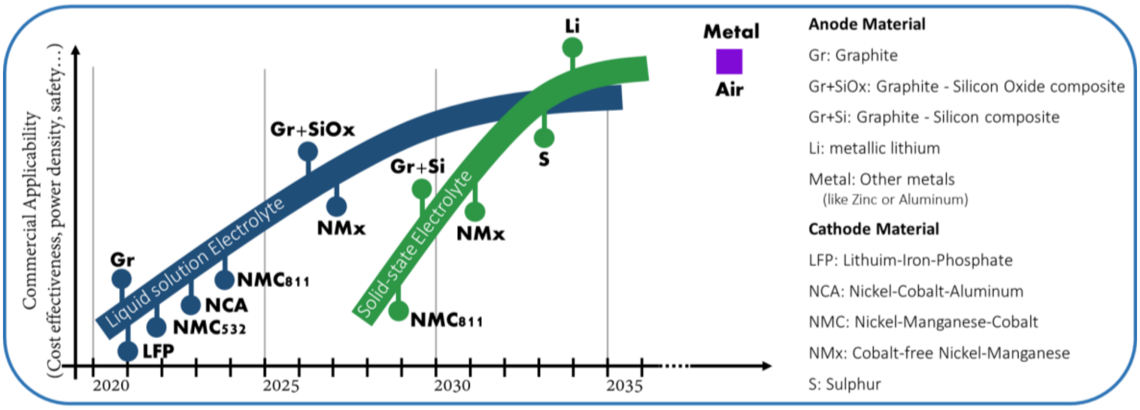

Figure 1 – Battery chemistry roadmap. Adapted from [23] and [24].

Despite of the advances on battery chemistry development, different issues are being reported such as market discontinuance [25] and raw-material limitations [26]. However, none of the previous issues is as concerning and crucial as the safety issues associated to battery electric vehicles [27]. Although BEVs are few worldwide compared to ICEs (expected to represent less than 7 % in 2030) [28], reports of battery failures leading to fire are increasing at a fast pace caused, to a great extent, by battery thermal runaway (BTR) issues [29]. The future increase of the BEV market share will require specific safety regulations for battery applications and advanced safety strategies to comply with them [30]. Therefore, it can be argued that the successful deployment of BEVs depends on a great extent in understanding the phenomenology related with the hazards that may occur and how to actuate in an effective manner to mitigate the problem or, at least, to provide a reliable approach that guarantees the driver's safety during situations that might originate battery combustion.

One of the most relevant descriptions of the thermal runaway phenomena to date is the one proposed by Golubkov et al. [31] and reinforced by the results from Zheng et al. [32] summarized in Figure 2. This approach was developed considering oven-like tests, in which the battery cell is submitted to a controlled heating procedure up to the point where it enters in thermal runaway. Initially, the battery is heated with very low heating rates (≈2°C to 5°C). Once the battery cell reaches temperatures around 100°C, the solid electrolyte interface (SEI) starts to decompose according to Richard and Dahn [33]. The decomposition of the metastable species has as outcome an appreciable energy release which increases the battery temperature [34]. The compounds released by the SEI decomposition such as ethylene carbonate (EC) reacts with the intercalated Lithium (Li^+) in the graphite in an exothermic way also assisting the temperature increase. On the other side of the SEI, the increase of the battery cell temperature also activates decomposition reactions in the cathode side. The temperature thresholds to enable the decomposition reaction are highly sensitive to the cathode chemistry in discussion (NMC, LCO, LFP, etc.)[35].

At temperatures of ≈160°C, the vent disc opening is observed which provides a temperature decrease from a Joule - Thompson effect, according to the authors [31]. Such statement is, however, only an assumption since they are not able to visualize the phenomena and relies only on temperature measurements. Other authors have highlighted that the venting of liquid phase materials may happen and have an important role on the thermal runaway occurrence [36]. On the other hand, the thermal runaway occurrence representation is still simplified, being considered as an abrupt increase of the temperature. The ignition location and development of the combustion process of the vent gas still lacks description.

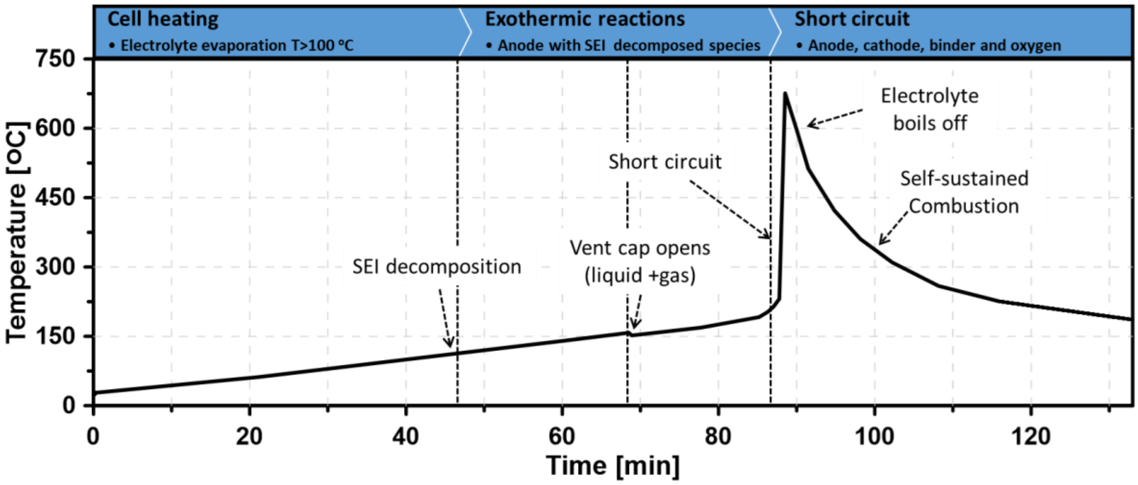

Figure 2 – Phenomenological description of battery thermal runaway.

Investigations aiming at identifying the composition of the vented gas were performed by different authors such as Sturk et al.[37]. Nonetheless, most of the studies doe not even refer to the different phases that may occur during the venting, which can dominate parameters as gas penetration, air entrainment, etc. It is evident that different points still need further discussions to improve the understanding of the thermal runaway phenomena. The characterization of the early venting phases is fundamental to correlate the mass loss, local heat transfer and the nature (liquid, gaseous or solid) of the ejected compounds. This mass loss and its nature (liquid, solid or gas) is of utmost importance to describe the occurrence of the thermal runaway phenomena since it dictates the remaining material inside of the battery cell and the concentration of each component. Next, the quantification of the time spent between the first visible material ejection and the flame initiation needs quantification, since it provides a way to developed safety-related measures. The flame initiation and propagation visualization can be the ultimate path to understand the phenomena and how to mitigate its propagation towards other battery cells. Moreover, the understanding of the flame shape and its evolution may allow to use combustion theory to model this phenomenon with high accuracy.

Therefore, in this study a Cobalt (LCO) chemistry was selected to understand the safety problems that can be found when is subjected to thermal abuse. This paper proposes to address these questions by means of combined thermodynamic and optical evaluations using a Li-ion battery cell Samsung ICR 18650 – 26 J, with LCO cathode chemistry. The effect of different heating rates by means of external air heating on the battery thermal runaway evolution is assessed using temperature evolution characterization, Schlieren visualization, Natural Luminosity and OH* radical tracing by an intensified camera with a 310 nm wavelength filter. This allows to create a visual description of the main external events that occurs in the battery thermal runaway (gas venting, flame initiation and development until extinction) and its correlation with the temperature of the battery cell. A Continuous Flow High Temperature Vessel (CFV) is used. The open volume test bed allows to increase the temperature under controlled conditions and evacuate the released gases, enhancing the visualization of the battery venting and combustion.

2. Experimental tools

This section intends to describe in detail the experimental facilities used during this investigation as well as the different optical techniques to assess the battery thermal runaway phenomenon.

2.1. Lithium Ion battery cell

For this study, Samsung ICR 18650 – 26 J cylindrical cells were used. Three fresh cells in identical conditions were tested in the Continuous Flow High Temperature Vessel. The battery state of charge (SOC) selected is 25% (3.58V) corresponding to level of charge that the cells are sold. In addition, the information of the current manuscript can help to understand the danger of storage of this type of cells as well as represents the BTR when the battery is in low charge conditions in a vehicle. The Samsung 26J is an 18650 (D=18 mm and L= 650 mm) battery with high power density typical used in devices like flashlights and power banks. The battery chemistry is defined as Lithium Cobalt Rechargeable (ICR) battery because use a Lithium Cobalt Oxide - $LiCoO_2$ cathode chemistry. The anode is composed by graphite as most of the lithium-ion cell of the market. The Samsung 26J cell is well known for having high specific energy thanks to its energy dense ICR chemistry. This battery boasts a 2,600mAh capacity which provides 215 Wh/kg. Additionally, the 26 J has a protection circuit board (PCB) that automatically detects and protects against overcharging, over discharging, and short circuiting due to BTR concerns. This cell has had multiple iterations since its release. These versions include, but are not limited to the 26F, 26H, 26M, and the 26J which is the current production version. It is important to note that the vent cap has 6 symmetrical distributed holes to release the cell pressure when is abused. This is important to characterize the venting process. In the market it is possible to found cells with 3 to 6 holes depending on the manufacturer. The main characteristics of the cell are presented in Table 1.

Table 1 – Main Lithium-Ion Samsung 26J battery cell properties.

Parameter	**Value**
Cell Origin	Purchase in free market
Cell format	18650
Dimensions [mm]	18.3 x 65.0
Weight [g]	44.6
Nominal Capacity [Ah]	2.6
Current Continuous/Peak [A]	5.6/10.3
Energy [Wh]	9.57
Power Continuous/Peak [W]	18.9/35.0
Energy density gravimetric [Wh/kg] / volumetric [Wh/L]	215/560
Power density gravimetric [W/kg] / volumetric [W/L]	785/2050
Vent Cap holes	6 holes
Voltage at 100% SOC [V]	4.02
Cut-off voltage [V]	2.75
Voltage for testing in CFV [V]	3.58 V
State of Charge for testing in CFV [%]	25

2.2. Continuous Flow Vessel and the Thermodynamic Characterization

A continuous Flow High Temperature Vessel (CFV) previously used for spray visualization of fuel injectors was adapted to work with lithium ion battery cells [38][39]. Figure 3 illustrates the experimental device used to perform the evaluation of thermal runaway under thermal abuse in this work. In addition, the vent cap scheme with the six holes can be seen in Figure 3 (CAD view). The facility is basically composed of four parts: gas compressors, gas heaters, test vessel and control system. The air is filtered, compressed, and stored in the high-pressure reservoirs. After lowering its humidity with a high-pressure industrial dryer, it enters the test chamber through a power regulated electric heating system (maximum of 30 kW). Hot gases exit the vessel and, after being cooled down, are ejected into the atmosphere. The vessel wall is composed by several layers which are aimed to decrease the heat transfer losses to the environment. Three quartz flat optical windows (no optical distortion) are included in the vessel with 90º between each to enable the application of different optical techniques simultaneously. Different thermocouples are included to monitor and acquire the temperature evolution in the battery cell, flow in, flow out and ambient vessel temperature. In addition, the volumetric flow rate is measured at the outside pipe of the CFV. Table 2 summarizes the main characteristic of the experimental setup and sensors used.

The test rig control system regulates both chamber temperature and pressure, where both signals are measured in the combustion chamber. Compared to similar test chambers, this chamber can reach temperatures up to 1100 K and internal pressure of 150 bar. The test section has a cubic shape of approximately 40 L in volume. The heaters are driven by a Proportional Integral Derivative control (PID) governed by a temperature set-point that is fixed at the desired level. Another PID system regulates the chamber pressure with a flow control valve that feeds the high-pressure air into the test chamber. The control system also manages safety checks, as minimum coolant flow, maximum heater output temperature, and a minimum gas flow value to protect the heaters. The chamber is optically accessible through three windows of 128 mm in diameter located in a line-of-sight arrangement, and one perpendicular to the axis of the battery cell. For this study, the latest mentioned window is replaced by a thermocouple support to measure battery cell wall temperatures. The main parameters of the CFV are depicted in [40].

To study the BTR, a support was built to maintain the cell in vertical position. In addition, the support protects the cell from the direct hot flow, increasing the homogeneity of the temperature in the cell. The support-cell was positioned in the lowest position to increase the field of view. The minimum volumetric flow and pressure was set in order to protect the heating resistance. Three heating ramps were proposed with differences of 3.5°C/min to understand the effect of the temperature in venting process and the combustion (7.5°C/min, 11.0°C/min and 14.5°C/min). This experiment maintains the heating ramp in all the process, different from an ARC where the cell is heated up to a set temperature and later the heating is done in small steps. The process methodology reduces drastically the test time compared to conventional Accelerated Rate Calorimeters (3 hours to 30 min) and ensure to achieve a high temperature to see the cell under thermal abuse. The heating ramp is maintained in all experiment. The end is marked when the cell reaches the ambient chamber temperature after the thermal runaway process.

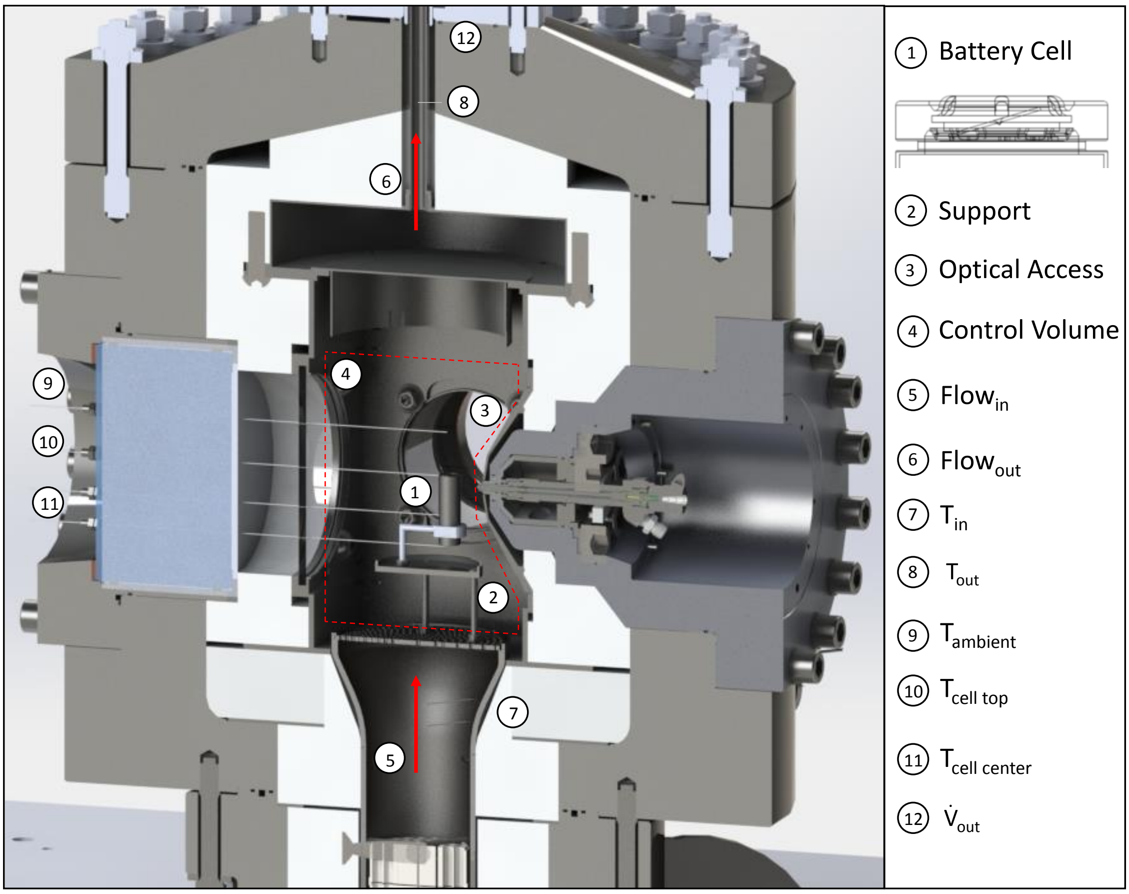

Figure 3 – Scheme of the experimental set up in the Continuous Flow Vessel (CFV).

Table 2 – Main test rig parameters.

Parameter	Value
Thermocouples Type K, 1 mm diameter and 300 mm length, Range [°C]	Up to 1100
Volumetric flow meter, Brooks Models SLA5863S, Flow rate [l/min]	0-2000
Chamber pressure sensor, WIKA IS-20-S-BBP, Pressure range [bar]	0-160
Continuous Flow Vessel Messkammer CMT from Advanced Combustion GmbH, max pressure [bar] and max chamber temperature [°C]	150/1373
Control Volume Size [L]	40
Heating resistance power [kW]	30
Volumetric flow during experiment [m^3/h]	54
Pressure during experiment [bar]	3.0
Heating ramp for thermal abuse [°C/min]	7.5, 11.0 and 14.5

To obtain more information about the combustion event, during thermal runway of the lithium-ion battery cell, the first law of thermodynamic (Eq. 1) is applied to the control volume (C.V) showed in Figure 3. The heat release of the cell ($\dot{Q}_{TR\,released}$) is obtained by the calculus of the energy variation components inside control volume (battery cell, battery support and chamber air) (Eq. 2), power inlet and outlet (Eq. 3) and the heat transfer to the walls (Eq. 4). The result is obtained after solve Eq. 5.

$$\frac{dE_{c.v}}{dt} = (\dot{E}_{in} - \dot{E}_{out}) - \dot{Q}_{losses} + \dot{Q}_{BTR\,released} \quad \text{(Eq. 1)}$$

$$\frac{dE_{c.v}}{dt} = m_{support} C_{p,support} \frac{dT_{suport}}{dt} + m_{cell} C_{p,cell} \frac{dT_{cell}}{dt} + m_{air} C_{p,air} \frac{dT_{air}}{dt} \quad \text{(Eq. 2)}$$

$$\dot{E}_{in/out} = \dot{m}_{in} C_{p,in/out} T_{in/out} \quad \text{(Eq. 3)}$$

$$\dot{Q}_{losses} = a\,T + b \quad \text{(Eq. 4)}$$

$$\begin{aligned} \dot{Q}_{BTR\,released} = {} & m_{support} C_{p,support} \frac{dT_{suport}}{dt} + m_{cell} C_{p,cell} \frac{dT_{cell}}{dt} + m_{air} C_{p,air} \frac{dT_{air}}{dt} \\ & - \dot{m}_{in} (C_{p,in} T_{in} - C_{p,out} T_{out}) \end{aligned} \quad \text{(Eq. 5)}$$

where E = energy, $\dot{E}$ = power, $\dot{Q}$ = heat variation, m = mass of the component, $\dot{m}_{in/out}$ = mass flow in the inlet/outlet, T= temperature and C_p = heat capacity at constant pressure. The support mass is $m_{support} = 474\ g$ with a $C_{p,steel} = 0.46 \frac{kJ}{kgK}$. The cell $C_{p,cell} = 1.06 \frac{kJ}{kgK}$ obtained by calorimetry test. The heat losses were correlated with the inside C.V temperature with stationary temperature test and validate with several ramp test without the battery cell. This allows to generate a correlation with a R^2 higher to 0.98. The values obtained are: $a = 0.0094 \frac{kW}{°C}\, and\ b = -0.2600\ kW$.

2.3. Optical techniques and Experimental Set Up

Three optical techniques were applied by the same optical access. Schlieren technique was used during the venting process to visualize the gas and liquid venting when the vent cap breaks up due excessive inside pressure. During the combustion, Natural Luminosity (NL) and OH*chemiluminescence tracking were applied.

The schlieren technique is based on the fact that when a light ray travels through a medium with refractive index gradients, it suffers a deflection due to the refraction phenomenon [41]. Accordingly, any variations of refractive index such as those produced by density variations at the vent gas can be recorded as different grey levels in an image. Consequently, this technique allows to observe the local density variations that the venting process provoke. The light generated by the light source passes through the vessel from one window to the other generating the density visualization in the schlieren camera. Two lenses were used to make the light parallel. The density visualization is achieved by the cut of the light by an iris diaphragm. The Natural luminosity signal corresponds to the thermal radiation emitted during the combustion process by the lithium ion cell [42]. It allows to analyse the flame propagation and stabilization during the thermal runaway. Spontaneous radiation emitted by the excited-state OH* molecules was used to visualize the near-stoichiometric high temperature zones, where combustion is taking place and soot oxidation is promoted. For this study, the experimental setup is shown in the scheme of Figure 4. The cameras are set in a triangle scheme to visualize by the same window. More details of the experimental set up is summarize in Table 3.

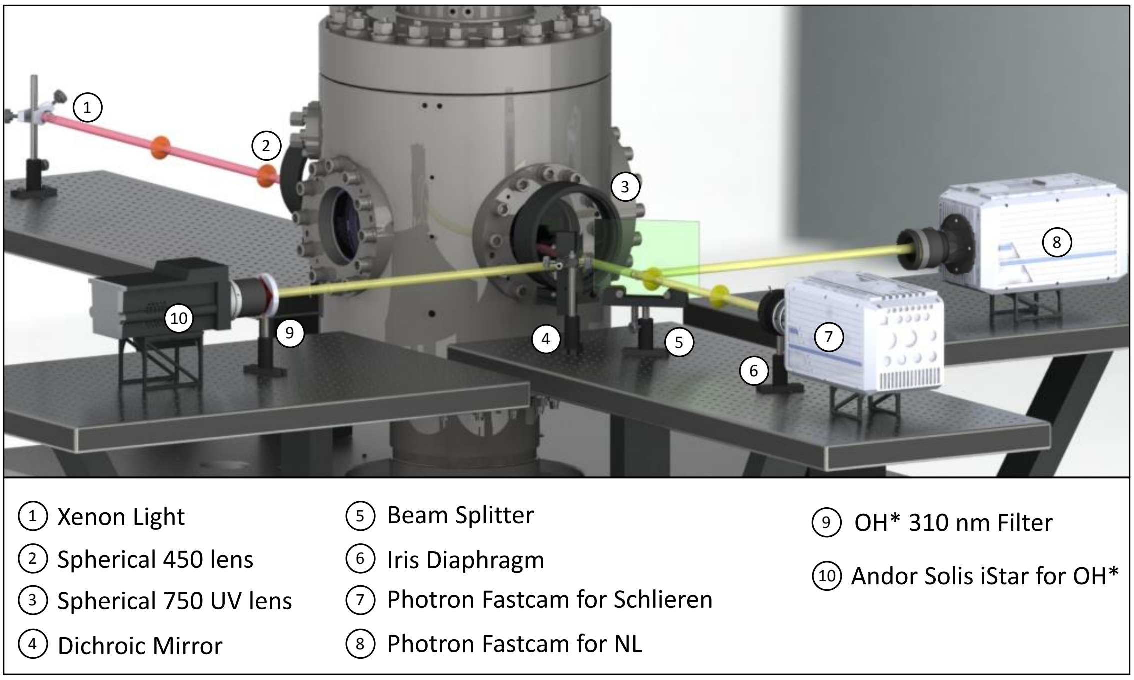

Figure 4 – Scheme of the optical techniques Continuous Flow Vessel (CFV).

Table 3 – Visualization components for Schlieren, Natural Luminosity and OH* tracking.

Component	Quantity	Specifications
High Speed Camera Photron Fastcam NOVA	*2*	*12-bit image, up to 16000 fps in max resolution.*
Andor Solis iStar DH334T-18H-83	*1*	*12-bit image, 5 fps and resolution 512x512, shutter speeds 0.2µs.*
Lens Carl Zeiss Makro-Planar	*2*	*Focal length 100 mm, f/2 lens*
Lens Nikon UV	*1*	*Focal length 105 mm, UV, f/4.5 lens*
OH Filter*	*1*	*310 nm ± 10 nm bandpass filter*
Dichroic Mirror	*1*	*Diameter 2 in, Reflection at 310 nm ≈ 98%. Transmission in visible (400-700 nm) ≈ 98%. Cut-Off Wavelength 805 nm.*
Beam splitter	*1*	*178x127 mm 50%T/50%R with a range from 450 to 750 nm.*
Light Source Karl Storz Nova 300	*1*	*Xenon lamp 300 Watts.*
Spherical lens	*1*	*f = 450 mm, D = 150 mm.*
Spherical UV lens	*1*	*f = 750 mm, D = 150 mm, UV.*
Iris diaphragm	*2*	*Metal iris diaphragm of diameter max 13 mm. Open diameter for experiment 5 mm.*

In order to have more details of the experimental set up, a description is presented.

Schlieren Technique

A high-speed single-pass schlieren imaging configuration was implemented to visualize the vent gas and liquid ejected when the pressure inside the cell brake the vent cap. On the illumination side, light from a xenon lamp is driven with a liquid light guide, to generate a point light source at the focal length plane of a spherical lens (f = 450 mm, D = 150 mm) so that the measurement area is illuminated with a collimated beam. The distance between the lens and the light is 450 mm and the distance between the lens and the CFV window is 5 mm. On the other side of the chamber, a spherical UV lens (f = 750 mm, D = 150 mm) was placed close to the optical access (5 mm of the CFV window). This lens focusses the light onto the Fourier plane where an iris diaphragm with a cut-off diameter of 5 mm was located. The distance between the UV lens and the iris diaphragm was 750 mm. A Photron Fastcam NOVA high speed CMOS camera was used to record the images with a rate of 12000 fps (0.083 ms) and positioned close to the iris diaphragm. The camera was equipped with a Carl Zeiss Makro-Planar T 100 mm f/2 ZF2 camera lens (Carl Zeiss, Aalen, Germany). The shutter time was 1.66 µs and it was kept constant throughout all the experiments. The resolution was 640 × 784 pixel with a total magnification of 6.8 pixel/mm. The schlieren images have been used to describe the venting process by differentiation of the gas venting and liquid venting. To obtain the precise moment of the venting an end trigger was used. The frame rate and resolution set allow 2.0 second of record images. Therefore, when the venting is seen in the monitor image, the trigger is sent. The previous 2.0 seconds contains the complete venting process desire to study. To quantify the process with values as spray distance and speed penetration, as well as angle of the spray a image postprocessing was done by an in-house MATLAB code that is capable to subtract the background and define the spray contours by threshold with 60% of the maximum light. More details about the code can be seen in previous publication of the research group in the field of injection process [43].

Natural Luminosity Technique

The Natural luminosity was recorded with a Photron Fastcam NOVA high speed CMOS camera with an exposure time of 0.208 µs and a frame rate of 6000 fps (0.166 ms) similar to the schlieren fast camera. A Carl Zeiss Makro-Planar T 100 mm f/2 ZF2 camera lens was mounted in the camera. The image resolution was 768x 720 pixels with a spatial resolution of 6.6 pixels/mm. As is positioned perpendicular to the field of view the cell image during combustion is possible due to a beam splitter 50% transmission and 50% reflection (percentage of the total light). The beam splitters reflect the light and is captured by a high-speed camera (like the schlieren fast camera but without any light cutting). Images were registered from the start of combustion by a manual trigger up to the end of combustion.

OH* Tracing Technique

In the case of the OH* an Andor Solis iStar DH334T-18H-83 intensified charged-coupled device (ICCD) camera was used. In addition, a Bernhard-Halle UV lens, with 100 mm focal length and f/4.5, and a 310 nm±10 nm band pass filter was mounted in the camera. A framerate of 4.17 images per second (0.24 ms between images) was used due to limitation of camera settings for the desire resolution. This means around 15 images during the combustion process of the cell due to a UV dichroic. The position is perpendicular to the field of view but before the NL camera. The light is reflected by a UV dichroic mirror with 98% of efficiency in the wavelength of 310 nm. Considering that the dichroic is transparent to the visible range (up to 750 nm), the NL camera not have distortion. The spatial resolution of the image was 8.75 pixel/mm and an exposure time of 500 µs to have a better defined image.

3. Results

The result section is divided into two different parts. First, the thermodynamic results are presented, illustrating the effect of the different heating rates on the temperature evolution and characteristic parameters of the thermal runaway process. Finally, the optical results from the schlieren, natural luminosity and OH radical are discussed in detail.

3.1. Thermodynamic Results

The battery cell is subjected to thermal abuse in three heating ramps (7.5°C/min, 11.0°C/min and 14.5°C/min) to understand the effect of the ambient temperature in the thermal runaway process. The test bed is controlled by the addition of power to the heating resistance in the intake pipe. The battery temperature inside of the HPHT is monitored to maintain the heating ramp constantly. Figure 5a show the temperature increases in the inside of the test bed chamber It is possible to see a suddenly increase of temperature. This is associated to the initiation of the combustion process. It is possible to know that there is a combustion due to the images later presented in the present manuscript (section 3.2). Before seen flames in the top of the cell (venting cap), there is a self-heating process where the battery temperature (in this work measured in the outside walls) overpass the ambient temperature (heating ramp produced by the CFV). This is due to the inside battery cell decomposition of SEI, cathode and anode. Therefore, the fuel gas vented by the cell and the hot temperature produce an initiation of the combustion. This all process is defined as thermal runaway The chamber temperature increase 50°C, 65°C and 70°C for the test 1 (7.5°C/min), test 2 (11.0°C/min) and test 3 (14.5°C/min), respectively. Figure 5b and Figure 5c shows the cell wall temperature in the center and top, respectively. These thermocouples show the venting process by a decrease of temperature. The liquid ejection when the vent cap opens due to excessive internal pressure, decrease the wall temperature. This is more noticeable in the top thermocouple than in the center due to the passage of the electrolyte by the vent cap orifices. The temperature decreases around 8.2°C in average for the three cases. The venting process cannot be detected with the thermocouple positioned in the HPHT ambient. As the time progresses, it is possible to see the thermal runaway process in which the temperature suddenly increases. Before the fast increase, the cell suffers self-heating (cell temperature increases higher than the ambient) due to exothermic reaction between cathode and anode. The electrolyte and SEI disappear leading to the cell short-circuit. The latest event is the cell cooling due to stop of heat release by thermal runaway process. So, the temperature is cooled by the test bed flow. The experiment is ended when the cell reaches the test bed chamber air temperature.

To complement the measurements, an energy balance is performed to obtain the heat release during thermal runaway. Figure 5d shows the heat release profile for the 11.0°C/min for brevity of the manuscript. The heat release (blue solid line) is calculated following Eq. 5, by the calculus of the battery cell, support and chamber air energy change and the power in the inlet, outlet and heat transfer. The latter is the main source of the heat release due to the increase of the energy outlet due to the high chamber temperature. In addition, the increase of the cell temperature (average wall temperature) absorb large part of the energy released in the battery thermal runaway event. The support and chamber air not have great influence due to the low increase of temperature and the total mass of the components. The total heat release is obtained as the final value accumulated. The results for the other cases are presented in Table 4.

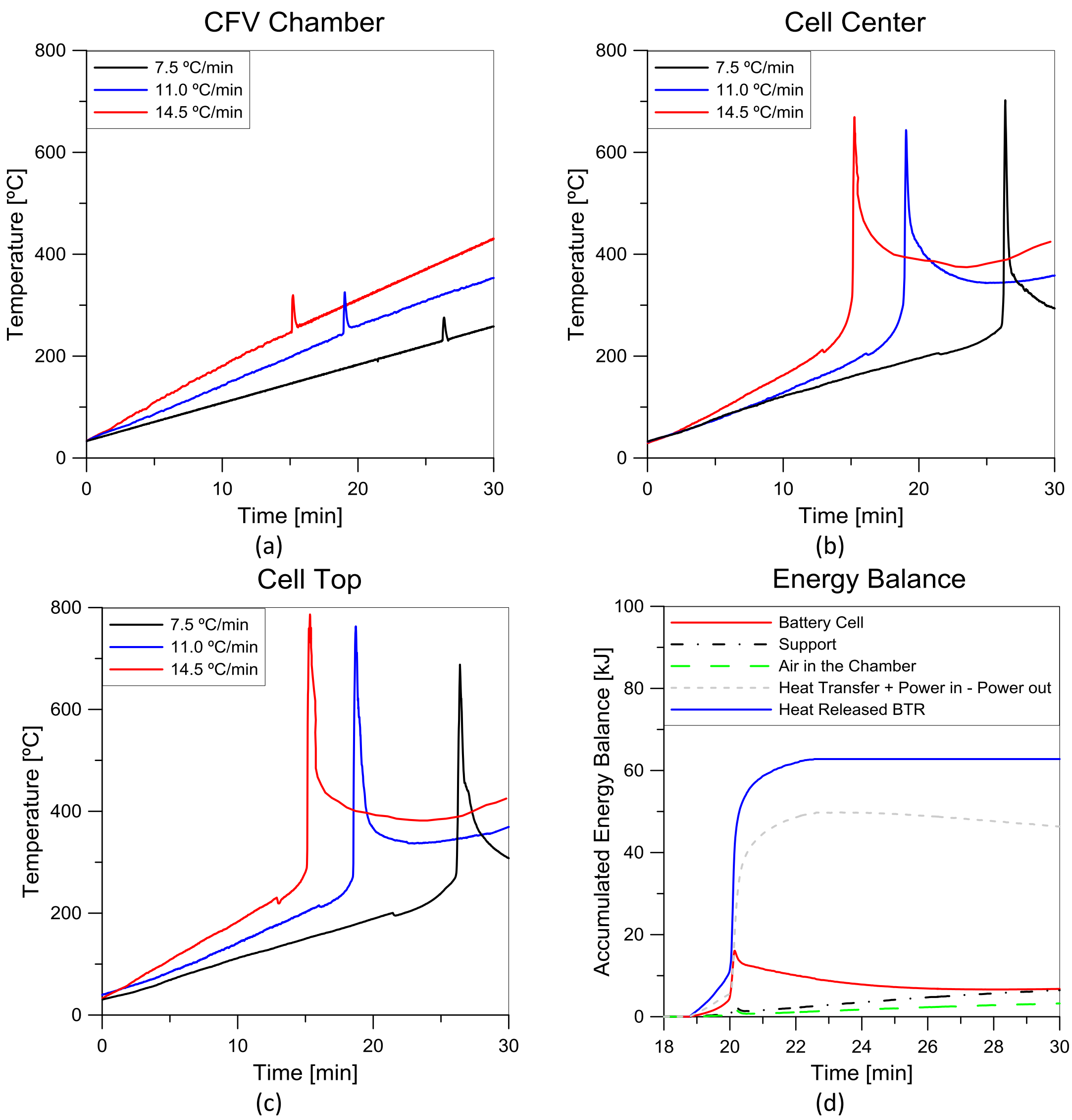

Figure 5 – Test bed HPHT ambient temperature (a), battery cell center temperature (b) and battery cell top temperature (c) for three heating ramps of 7.5°C/min, 11.0°C/min and 14.5°C/min. In addition, energy balance for the calculation of heat release during thermal runaway for case 11.0°C/min.

In addition, Table 4 shows some of the characteristic parameters of the battery thermal runaway event for the different heating ramps. As it is shown, the increase of heating ramp has a low influence in the venting start temperature with a difference of 13°C between extreme cases (5% of the onset temperature). However, the trend seen is that with the increase of the heat ramp, the venting is delayed. This phenomenon may be explained by the heat diffusion towards the battery center. Despite having higher heating rates, the heat transfer is limited by the thermal properties of the battery cell. In this sense, it is suggested that the cell interior temperature may have much lower differences than those presented by the surface. The time difference between venting is of 4.9 min between the two first cases and 6.1 min between the second and third case (11.1 min between extreme cases). An additional important parameter to be considered is the time between the venting and smoke event (just before the peak of temperature). In this work it is defined as safety time because it can be used to prevent the fire of the cell if the venting is detected or to warn the people to leave the vehicle. This time decrease with the heating ramp as expected due to the ambient temperature. However, an interesting result is the reduction from 11.0°C/min to 14.5°C/min (0.31 min) with respect to 7.5°C/min to 11.0°C/min (2.15 min). This result suggests that the safety time has a non-linear dependence with the heating rate. Therefore, this behavior must be accounted in the safety system of the vehicles. It is suggested that the extension of the investigations regarding safety time characterization could be a pathway to reduce the hazards associated with battery combustion.

Table 4 – Main parameter of thermal runaway by thermal abuse.

Parameter	**7.5°C/min**	**11.0°C/min**	**14.5°C/min**
Temperature venting [°C]	201.1	215.8	230.9
Time of venting process [min]	21.38	16.04	12.85
Temperature decreases during venting [°C]	7.2	4.5	11.7
Temperature smoke [°C]	274.4	281.7	287.6
Time of smoke event [min]	25.99	18.71	14.85
Maximum Temperature achieved [°C]	686.9	763.0	787.0
Time of maximum Temperature achieved [min]	26.29	18.94	15.15
Safety Time [min]	4.68	2.54	2.23
Heat Released [KJ]	61.2	62.7	65.5
Cell mass after experiment [g]	38.64	38.53	38.75

*Temperature referred of the cell top

3.2. Visualization Results

The visualization results are split in three techniques (schlieren and natural luminosity with a fast camera and OH* track by a 310nm filter in an intensified camera). The first abovementioned technique is used during venting process and the other two during the combustion process. As presented in the previous subsection, the venting was previously seen as a decay of cell wall temperature and combustion process by a suddenly increase of cell wall temperature and ambient temperature.

Venting Process

The venting is shown in Figure 6 in two sequences. The first sequence shows the initial part of the event from 0 to 7 ms (Figure 6a). The images were taken with a frequency of 0.083 ms. Nonetheless, for brevity of the manuscript only a step of 0.5 ms is depicted. The initial phase is predominant by liquid phase (high light absorption). Since a 6 holes battery vent cap is used (Figure 3), the jets are superimposed in the schlieren view. In the first 3 ms, it is possible to clearly see 4 jets (the other two are behind) growing. Around the time of 5 ms, the venting spray reaches the optical window, and the spray is more uniform and intense than in the first 4 ms. Figure 6b shows the same event with a timestep of 10 ms, to have an overview of all the process. The first 10 ms is predominant liquid phase, follow by a mix of liquid and gas and lastly only gas ejection (before 40 ms). Between the instant 20 to 50 ms is possible to see a solid attached to the vent cap in the same direction of the liquid jet. It is believed that this solid material can be originated from the melting of the separator. Nonetheless, further investigations will be performed by collecting the remaining material to understand the nature of the solid material ejected during the venting process. The last image taken in the schlieren camera was 140 ms after the first venting optical signal due to limitation of the camera memory. However, the venting process continues up to the combustion phase with low intensity, i.e., with a similar shape of that presented in the last image of Figure 6b.

The images were postprocessed with an in-house MATLAB code to obtain the contour of the jets. The position of the furthest point was traced to obtain penetration distance and speed. In addition, the angle of the spray was also obtained. The values represent the angle between the centroid of the jet (area inside of the contour) and the horizontal plane (90° to the vertical axle of the cell). The results are presented in Table 5 for brevity of the manuscript. Up to 3 ms there is not wall effect on the spray and the penetration can be obtained. The speed of the spray in the CFV chamber was around 18 m/s in the first instance and achieve 30 m/s after 2 ms of start of injection. The angle is high at the beginning (close to the horizontal) and after 3 ms start to be more vertical to arrive at the end of the liquid phase with an angle of 40°. Small differences were seen between the right and left sprays.

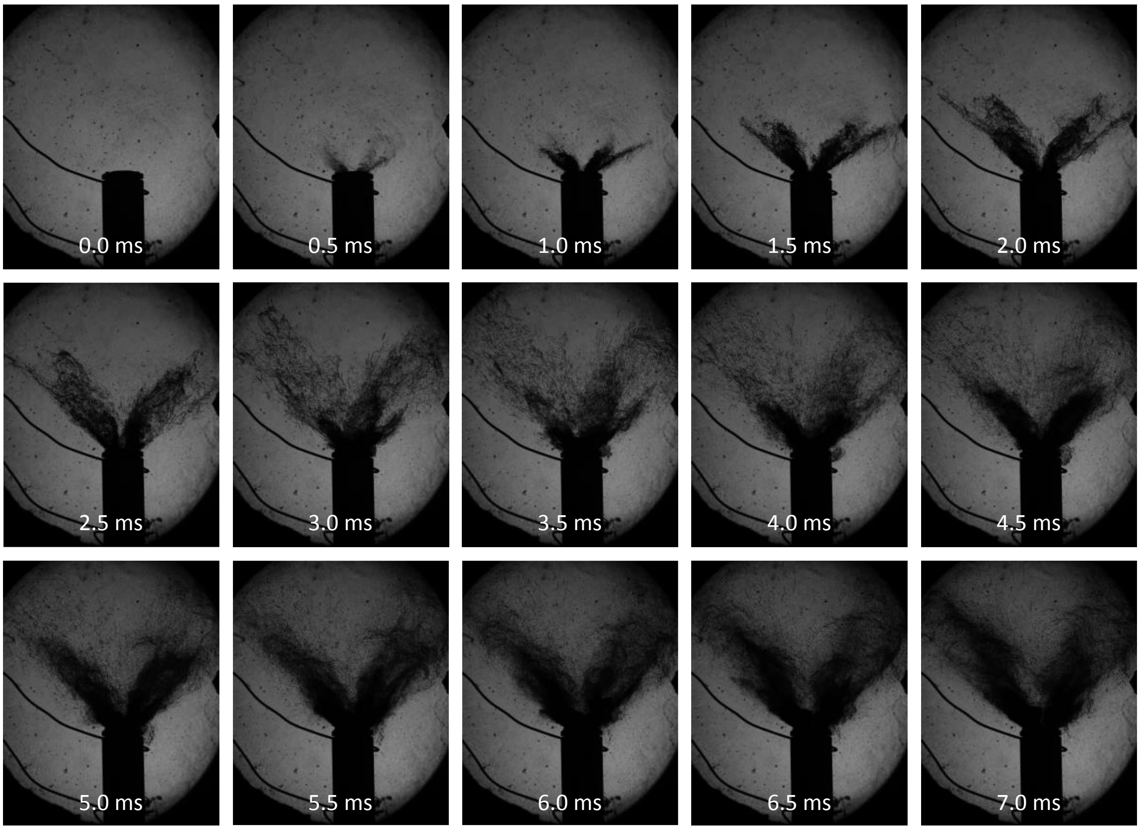

(a)

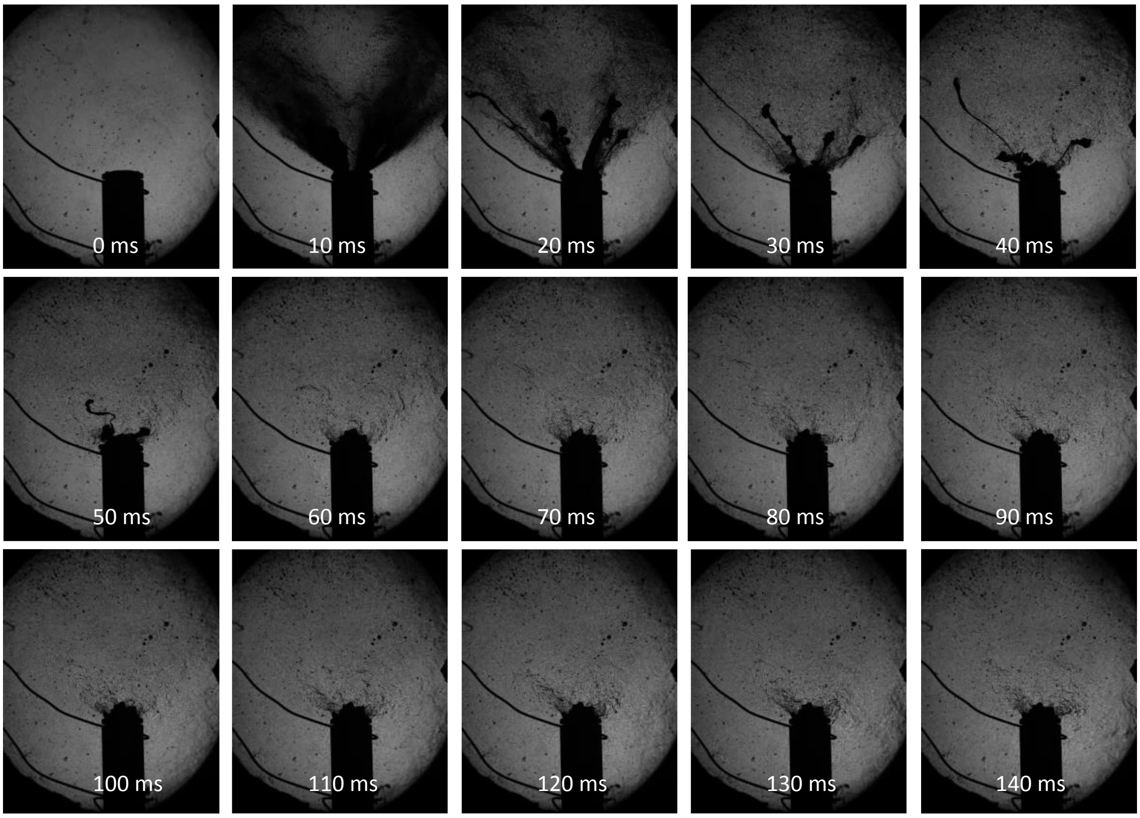

(b)

Figure 6 –Schlieren Technique for venting process with 0.5 ms (a) and 10 ms (b). Case 11.0°C/min, Temperature chamber ≈ 230°C, Temperature Cell Top ≈ 226°C, Temperature Cell center ≈ 206°C.

Table 5 – Main parameter of thermal runaway by thermal abuse.

Parameter	**1ms**	**1.5ms**	**2ms**	**2.5ms**	**3ms**	**3.5ms**	**4ms**	**6ms**	**8ms**	**10ms**
Spray Penetration Distance Right [mm]	18.0	30.7	43.8	51.1	61.3	-	-	-	-	-
Spray Penetration Speed Right [m/s]	18	25	26	15	20	-	-	-	-	-
Spray Penetration Distance Left [mm]	18.4	28.1	45.4	51.1	66.7	74.8	-	-	-	-
Spray Penetration Speed Left [m/s]	18	19	35	11	31	16	-	-	-	
Spray Angle Right [deg]	53	54	49	42	36	34	41	34	36	40
Spray Angle Left [deg]	33	49	44	42	39	34	47	40	45	46

Combustion Process

The natural luminosity images allow to garner information about the combustion process by the light emitted by the flame. It is important to note that previously to the combustion event, around of 1 second of smoke is produced by the cell. This is possible to note in the first 20 ms of NL images (Figure 7a). The images show two separate flames coming from left and right vent cap holes. As the vent cap rupture is not uniform, the flame angle differs despite the symmetry of the hole distribution on the flame. The right side of the cell has sharper angle with respect to the vertical plane. This is maintained in all the combustion process. Therefore, the vent cap disc does not change the position during the event.

Figure 7b shows the same event with a timestep of 100 ms to appreciate the initial phase up to the extinction of the flame. The process has a duration of 1.4 seconds with the first 0.3 seconds of intense flame and the other with a shorter flame with less emitted light. This means less temperature and soot formation. The Figure 7c shows the OH* images taken with the ICCD + 310 nm filter during the combustion process. The process shows a weak signal of OH* chemiluminescence radiation, with an increase of the signal close to the battery cell for 240, 480 and 720 ms. This could be associated with two main factors. The first one is related with the intensifier capabilities that are not able to register this low OH* intensity. Therefore, the OH* chemiluminescence radiation was not registered by the camera. The second factor is related with the attenuation of the OH* signal due to the high soot concentration during the BTR. This effect was already seen in Diesel ICE combustion in a previous works of the research group [42]. For future work is proposed emission spectroscopy to track the species generated in the combustion under thermal abuse.

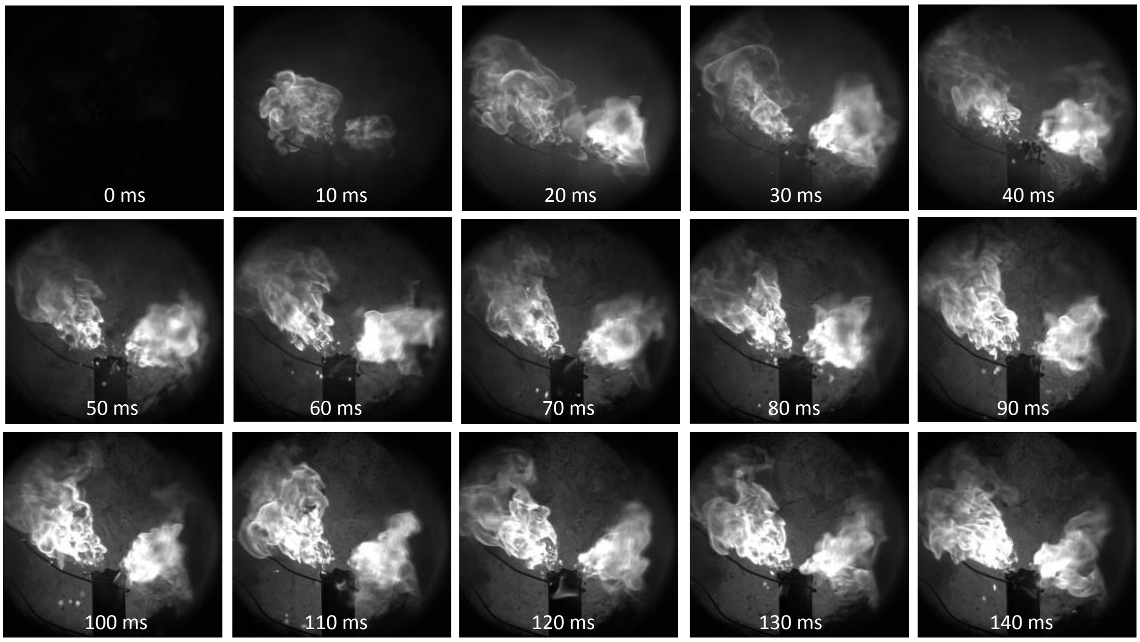

(a)

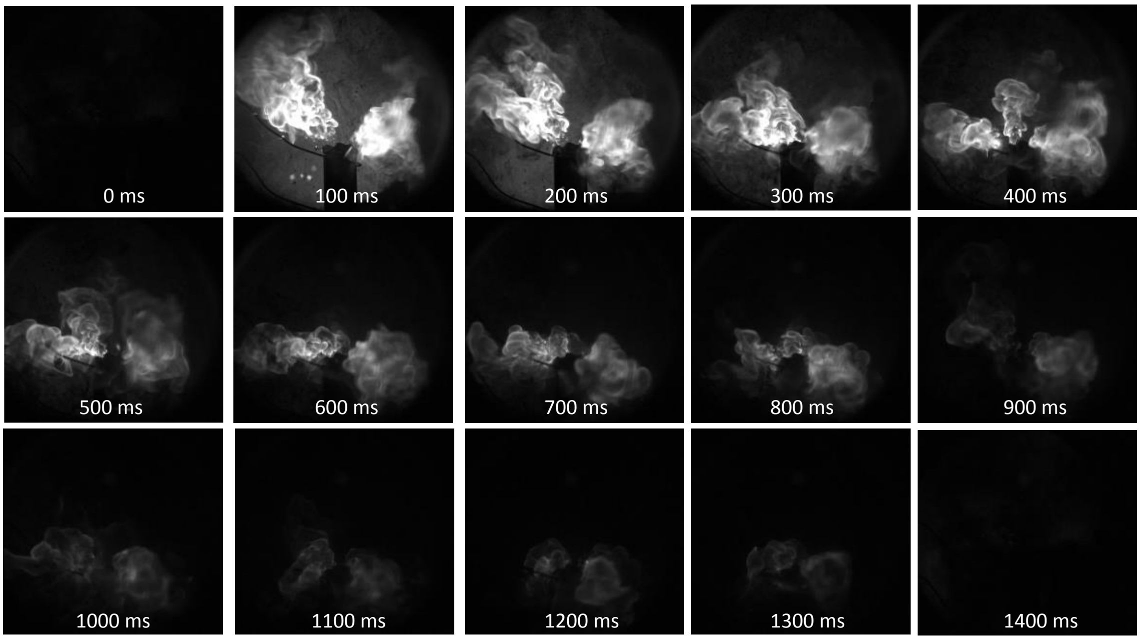

(b)

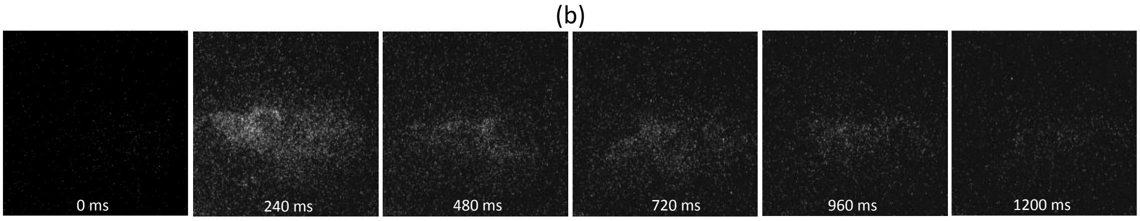

(c)

Figure 7 – Natural Luminosity with 10 ms (a) and 100 ms (b) and OH* images (c). Case 11.0°C/min, Temperature chamber ≈ 243°C, Temperature Cell Top ≈ 300°C, Temperature Cell center ≈ 270°C.

Considering the previous results, a graphical description of the battery thermal runaway process can be developed. Initially, the cell is heated by means of an external heat source until the temperature threshold for SEI decomposition is obtained. The following increase in the temperature is a consequence of both the external heating and the exothermic reactions that starts to occur inside of the battery cell. This leads to a gas generation that starts to increase the inner battery pressure up to the point where the vent cap is partially break up, releasing a small concentration of gas. This process is followed by a significant liquid ejection from the battery. Such phenomenon was still not investigated in detail up to now. Despite of the low duration of liquid ejection compared to the whole battery venting process (10 ms versus 140 ms), it is suggested that the mass loss during this phase is comparable to the rest of the whole venting process since the density of the liquid ejected benefits the mass loss during the early phases.

Next, the battery cell remains venting for a period up to the point where the temperature provides the energy to auto ignite the gases. The autoignition is generally related with the time where the short-circuit occurs. The flame starts to propagate around the battery, forming a well-defined structure that lasts more than one second. This result differs from other authors that reports the battery thermal runaway process as an explosion[44]. These results open the path to use the combustion theory from premixed and diffusive flames to model the combustion evolution during the thermal runaway. It is important to remark that other secondary phenomena were also evidenced such as the ejection of flammable solids from the battery that can be forwarded outside of the flame as it shown in the fifth frame of Figure 8. Finally, as the reactants are consumed, the reaction rates start to decrease, leading to the extinction of the oxidation process as shown in frame six.

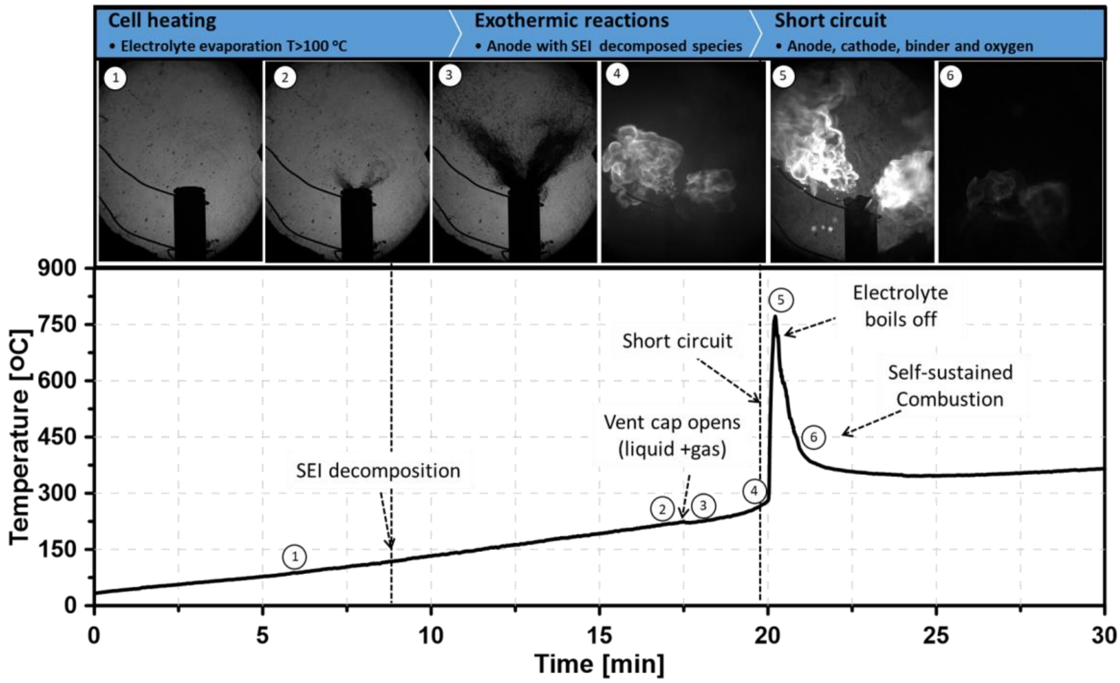

Figure 8 – Novel graphical battery thermal runaway description considering the results form Schlieren and natural luminosity.

4. Conclusion

This work has investigated in detail the battery thermal runaway phenomena of LCO 18650 cylindrical battery cell using a novel continuous flow high temperature vessel together with advanced optical techniques. The novel assessment device allowed to visualize in detail the BTR phenomenon, since its continuous flows removes the smoke that is originated during the process and generally hinders the applications of optical techniques in devices such as accelerated rate calorimeter. The findings of the investigation have allowed to shed light on important phenomena that occurs during the thermal runaway such as:

- The evolution of the temperature profiles has demonstrated a lower dependence between the venting characteristic temperatures and the heating ramp used to heat up the battery cell as the ramp temperature levels are increased. The same can be extended to the maximum temperature achieved.

- The schlieren visualization evidenced the high amount of liquids ejected in the early phases of the venting process followed by a period of gaseous venting. This finding highlights the complexity of the thermal runaway phenomena, but also provides a reliable description of the phenomena and how to obtain an accurate modelling of the venting process by means of 3-D CFD simulations.

- Combustion process was characterized, concluding that its shape and evolution has several similarities to those of controlled flames from conventional turbulent burners. This may allow to use conventional representation from combustion process to model the battery combustion during thermal runaway.

It is worth to note that the discussion presented in the manuscript also allowed to highlight important phenomena such as the interplay between the nozzle velocity and spray angle inclination that dictates the equivalence ratio field near to the battery and also the entrained mixture by the flame. This can support the improvement of modelling approaches to accurate describe the combustion propagation. In addition, it may open the path to use modelling approaches such as the weighted-multi-point-source-model (WMP) for radiative heat transfer for the other cells as well as to validate velocity fields that may affect the convective heat transfer. In this sense, it can be concluded that the extension of traditional optical techniques previously used for combustion-based investigation is a powerful tool to garner insights on battery-related phenomena as the thermal runaway. Using these tools, a graphical description was attained, which can be used to develop better predictive TR models and understand the evolution of this hazard towards other cells. Further investigation on quantifying not only the geometric parameters but also the composition aspects of the process are needed to provide a closed problem that can be used to simulate in detail the thermal runaway process.

5. Abbreviations

LFP	Lithium *Ferrum* Phosphate	ICR	Lithium Cobalt Rechargeable
BEV	Battery Electric Vehicles	LCO	Lithium Cobalt Oxide
BTR	Battery Thermal Runaway	Li	Lithium Ferrum Phosphate
C.V	Control Volume	mm	Millimeter
CFV	Continuous Flow Vessel	ms	Millisecond
deg	Degree	NCA	Nickel Cobalt Aluminium Battery Cell Cathode Material
f	Focal Length	NL	Natural Luminosity
f/	Focal Number	nm	Nanometer
fps	Frame Per Second	NMC	Nickel Manganese Cobalt Battery Cell Cathode Material
Gr	Graphite	OH*	OH Radical
Gr+SiOx	Graphite And Silicon Oxide Composite	S	Sulphur
ICCD	Intensified Charged-Coupled Device	SEI	Solid Electrolyte Interface
ICE	Internal Combustion Engine	UV	Ultra Violet
ICEVs	Internal Combustion Engine Vehicles		

6. Acknowledgments

Operación financiada por la Unión Europea a través del Programa Operativo del Fondo Europeo de Desarrollo Regional (FEDER) de la Comunitat Valenciana 2014-2020 con el objetivo de promover el desarrollo tecnológico, la innovación y una investigación de calidad. Proyecto IDIFEDER/2021/053, Equipamiento para el estudio del fenómeno de combustión no controlada en baterías de vehículos eléctricos, entidad beneficiaria Universitat Politècnica de València.

7. References

[1] IEA, "A Roadmap for the Global Energy Sector," p. 222, 2021.

[2] J. Benajes, A. García, J. Monsalve-Serrano, and S. Martínez-Boggio, "Potential of using OMEx as substitute of diesel in the dual-fuel combustion mode to reduce the global CO2 emissions," *Transp. Eng.*, vol. 1, no. January, p. 100001, 2020.

[3] A. García, J. Monsalve-Serrano, D. Villalta, R. Lago Sari, V. Gordillo Zavaleta, and P. Gaillard, "Potential of e-Fischer Tropsch diesel and oxymethyl-ether (OMEx) as fuels for the dual-mode dual-fuel concept," *Appl. Energy*, vol. 253, no. May, p. 113622, 2019.

[4] A. García, J. Monsalve-Serrano, S. Martínez-Boggio, V. Rückert Roso, and N. Duarte Souza Alvarenga Santos, "Potential of bio-ethanol in different advanced combustion modes for hybrid passenger vehicles," *Renew. Energy*, vol. 150, pp. 58–77, 2020.

[5] R. L. Sari, D. Golke, H. J. Enzweiler, N. P. G. Salau, F. M. Pereira, and M. E. S. Martins, "Exploring optimal operating conditions for wet ethanol use in spark ignition engines," *Appl. Therm. Eng.*, vol. 138, 2018.

[6] A. García, J. Monsalve-Serrano, R. Lago Sari, and P. Gaillard, "Assessment of a complete truck operating under dual-mode dual-fuel combustion in real life applications: Performance and emissions analysis," *Appl. Energy*, vol. 279, no. September, p. 115729, 2020.

[7] Y. Zhang and M. Sellnau, "A Computational Investigation of PPCI-Diffusion Combustion Strategy at Full Load in a Light-Duty GCI Engine," *SAE Tech. Pap. Ser.*, vol. 1, pp. 1–19, 2021.

[8] A. García, J. Monsalve-Serrano, R. Lago Sari, and S. Martinez-Boggio, "Energy assessment of an electrically heated catalyst in a hybrid RCCI truck," *Energy*, vol. 238, p. 121681, 2022.

[9] T. Liu, Y. Liu, X. Wang, X. Kong, and G. Li, "Cooling control of thermally-induced thermal runaway in 18,650 lithium ion battery with water mist," *Energy Convers. Manag.*, vol. 199, no. August, p. 111969, 2019.

[10] International Energy Agency (IEA), "Global EV Outlook 2020: Entering the decade of electric drive?," *Glob. EV Outlook 2020*, p. 273, 2020.

[11] R. Gozdur, B. Guzowski, Z. Dimitrova, A. Noury, G. Mitukiewicz, and D. Batory, "An energy balance evaluation in lithium-ion battery module under high temperature operation," *Energy Convers. Manag.*, vol. 227, p. 113565, 2021.

[12] T. Katrašnik, I. Mele, and K. Zelič, “Multi-scale modelling of Lithium-ion batteries: From transport phenomena to the outbreak of thermal runaway,” *Energy Convers. Manag.*, vol. 236, 2021.

[13] K. Liu, X. Hu, Z. Yang, Y. Xie, and S. Feng, “Lithium-ion battery charging management considering economic costs of electrical energy loss and battery degradation,” *Energy Convers. Manag.*, vol. 195, no. April, pp. 167–179, 2019.

[14] Y. Baik, R. Hensley, P. Hertze, and S. Knupfer, “Making electric vehicles profitable,” *McKinsey Co.*, no. March, 2019.

[15] “Battery Pack Prices Cited Below $100/kWh for the First Time in 2020, While Market Average Sits at $137/kWh | BloombergNEF.” [Online]. Available: https://about.bnef.com/blog/battery-pack-prices-cited-below-100-kwh-for-the-first-time-in-2020-while-market-average-sits-at-137-kwh/. [Accessed: 29-Mar-2021].

[16] A. Masias, J. Marcicki, and W. A. Paxton, “Opportunities and Challenges of Lithium Ion Batteries in Automotive Applications,” *ACS Energy Lett.*, vol. 6, no. 2, pp. 621–630, Feb. 2021.

[17] S. Dhundhara, Y. P. Verma, and A. Williams, “Techno-economic analysis of the lithium-ion and lead-acid battery in microgrid systems,” *Energy Convers. Manag.*, vol. 177, no. September, pp. 122–142, 2018.

[18] EUCAR, “Battery requirements for future automotive applications,” *Eg Bev&Fcev*, no. July, pp. 1–18, 2019.

[19] J. Wang and X. Sun, “Olivine LiFePO4: The remaining challenges for future energy storage,” *Energy Environ. Sci.*, vol. 8, no. 4, pp. 1110–1138, 2015.

[20] L. Sheng, L. Su, H. Zhang, Y. Fang, H. Xu, and W. Ye, “An improved calorimetric method for characterizations of the specific heat and the heat generation rate in a prismatic lithium ion battery cell,” *Energy Convers. Manag.*, vol. 180, no. November 2018, pp. 724–732, 2019.

[21] J. Sun, Z. Li, X. Ren, L. Wang, and G. Liang, “High volumetric energy density of LiFePO4/C microspheres based on xylitol-polyvinyl alcohol complex carbon sources,” *J. Alloys Compd.*, vol. 773, pp. 788–795, 2019.

[22] Y. Wang, S. Song, C. Xu, N. Hu, J. Molenda, and L. Lu, “Development of solid-state electrolytes for sodium-ion battery-A short review,” *Elements*, vol. 1, no. 2, pp. 91–100, 2021.

[23] Volkswagen., “Powerful and scalable: the new ID. Battery system,” 2018. .

[24] M. Meeus, “Overview of Battery Cell Technologies - European Battery Cell R&I Workshop,” 2018.

[25] S. Hardman and G. Tal, “Understanding discontinuance among California’s electric vehicle owners,” *Nat. Energy*, vol. 6, no. 5, pp. 538–545, 2021.

[26] International Energy Agency (IEA), “The Role of Critical Minerals in Clean Energy Transitions,” *IEA Publ.*, 2021.

[27] P. Sun, R. Bisschop, H. Niu, and X. Huang, *A Review of Battery Fires in Electric Vehicles*, vol. 56, no. 4. Springer US, 2020.

[28] K. M. Tsang, L. Sun, and W. L. Chan, “Identification and modelling of Lithium ion battery,” *Energy Convers. Manag.*, vol. 51, no. 12, pp. 2857–2862, 2010.

[29] R. Bisschop, O. Willstrand, F. Amon, and M. Rosengren, *Fire safety of lithium-ion batteries in road vehicles, RISE Report 2019:50*. 2019.

[30] Y. Xie *et al.*, “Experimental and numerical investigation on integrated thermal management for lithium-ion battery pack with composite phase change materials,” *Energy Convers. Manag.*, vol. 154, no. October, pp. 562–575, 2017.

[31] A. W. Golubkov *et al.*, “Thermal-runaway experiments on consumer Li-ion batteries with metal-oxide and olivin-type cathodes,” *RSC Adv.*, vol. 4, no. 7, pp. 3633–3642, 2014.

[32] S. Zheng, L. Wang, X. Feng, and X. He, “Probing the heat sources during thermal runaway process by thermal analysis of different battery chemistries,” *J. Power Sources*, vol. 378, no. July 2017, pp. 527–536, 2018.

[33] M. N. Richard and J. R. Dahn, “Accelerating rate calorimetry studies of the effect of binder type on the thermal stability of a lithiated mesocarbon microbead material in electrolyte,” *J. Power Sources*, vol. 83, no. 1–2, pp. 71–74, 1999.

[34] A. Kriston, I. Adanouj, V. Ruiz, and A. Pfrang, “Quantification and simulation of thermal decomposition reactions of Li-ion battery materials by simultaneous thermal analysis coupled with gas analysis,” *J. Power Sources*, vol. 435, no. June, pp. 1–13, 2019.

[35] A. García, J. Monsalve-Serrano, R. Lago Sari, and Á. Fogué Robles, “Numerical analysis of kinetic mechanisms for battery thermal runaway prediction in lithium-ion batteries,” *Int. J. Engine Res.*, p. 146808742110299, 2021.

[36] P. T. Coman, S. Rayman, and R. E. White, “A lumped model of venting during thermal runaway in a cylindrical Lithium Cobalt Oxide lithium-ion cell,” *J. Power Sources*, vol. 307, pp. 56–62, 2016.

[37] D. Sturk, L. Rosell, P. Blomqvist, and A. A. Tidblad, “Analysis of li-ion battery gases vented in an inert atmosphere thermal test chamber,” *Batteries*, vol. 5, no. 3, pp. 1–17, 2019.

[38] R. Payri, J. S. Giraldo, S. Ayyapureddi, and Z. Versey, “Experimental and analytical study on vapor phase and liquid penetration for a high pressure diesel injector,” *Appl. Therm. Eng.*, vol. 137, no. March, pp. 721–728, 2018.

[39] R. Payri, F. J. Salvador, R. Abboud, and A. Viera, “Study of evaporative diesel spray interaction in multiple injections using optical diagnostics,” *Appl. Therm. Eng.*, vol. 176, no. May, p. 115402, 2020.

[40] R. S. G. Baert, P. J. M. Frijters, B. Somers, C. C. M. Luijten, and W. De Boer, “Design and operation of a high pressure, high temperature cell for HD diesel spray diagnostics: Guidelines and results,” *SAE Tech. Pap.*, 2009.

[41] J. V. Pastor, A. García, C. Micó, and A. A. García-Carrero, “Experimental study of influence of Liquefied Petroleum Gas addition in Hydrotreated Vegetable Oil fuel on ignition delay, flame lift off length and soot emission under diesel-like conditions,” *Fuel*, vol. 260, no. July 2019, p. 116377, 2020.

[42] J. V. Pastor, A. García, C. Micó, and F. Lewiski, “Simultaneous high-speed spectroscopy and 2-color pyrometry analysis in an optical compression ignition engine fueled with OMEX-diesel blends,” *Combust. Flame*, vol. 230, no. x, 2021.

[43] R. Payri, J. M. García-Oliver, M. Bardi, and J. Manin, “Fuel temperature influence on diesel sprays in inert and reacting conditions,” *Appl. Therm. Eng.*, vol. 35, no. 1, pp. 185–195, 2012.

[44] Y. Chen *et al.*, “A review of lithium-ion battery safety concerns: The issues, strategies, and testing standards,” *J. Energy Chem.*, vol. 59, pp. 83–99, 2021.